

Universität Zürich[UZH]

University of Zurich

Bachelor Thesis

The Impact of Supermassive Black Holes on Galaxy Morphology

Author:
Mila Lüscher

Supervisors:
Prof. Dr. Romain Teyssier
Michael Kretschmer

May 21, 2021

Acknowledgement

First of all, I would like to thank Prof. Dr. Romain Teyssier for taking me under his wing and introducing me to the world of computational astrophysics. When I first contacted him I mentioned my fascination with black holes and my enthusiasm for learning more in the field of coding. He immediately had an idea for a project, which I got excited by and to this day still am. I am also grateful for the freedom I was given to pursue my own ideas and questions.

I would also like to thank Michael Kretschmer for helping me out with the analysis of the data. He was always very patient and quick to respond to any (sometimes very trivial) questions I had. Coding is hard and even more so when you have to debug certain issues for the first time. I am sure that if it wasn't for Michael my experience writing this thesis would not have been as joyous as it was. I could have not done it without his help.

Abstract

This paper deals with the impact supermassive black holes (SMBH) have on the evolution and morphology of galaxies. Three cosmological simulations were performed with the adaptive mesh refinement (AMR) hydrodynamical code RAMSES. Two of the simulations had SMBH's implemented in the form of sink particles, whereas the third had none. Turbulence was resolved in the SMBH Bondi accretion process for one of the two sink particle simulations.

For the analysis of the galaxies, a Sérsic profile was fit to the stellar and cold gas mass. Furthermore, the orbital circularity of the stellar mass was probed to further determine the structure of the galaxies. In addition, the SMBH behaviour of the sink particle simulations was evaluated. It was found that the galaxies with SMBH sink particles implemented were ellipticals whereas the non-SMBH galaxy was more of a spiral nature with an uncharacteristically large bulge. Adding turbulence to the accretion process seemed to delay the SMBH mass accretion and hence allows more time for star formation which leads to brighter galaxies.

Contents

1 Theory **4**
- 1.1 An Overview of Galaxy Formation . . . 4
- 1.2 Galaxy Morphology . . . 5
  - 1.2.1 Elliptical Galaxies . . . 5
  - 1.2.2 Spiral Galaxies . . . 6
  - 1.2.3 Lenticular Galaxies . . . 6
- 1.3 Supermassive Black Holes . . . 6
  - 1.3.1 Formation . . . 7
  - 1.3.2 Accretion . . . 7
  - 1.3.3 Active Galactic Nuclei and Feedback . . . 8

2 Computational Techniques **9**
- 2.1 Ramses . . . 9
  - 2.1.1 Hydrodynamics with Adaptive Mesh Refinement . . . 9
  - 2.1.2 Cosmological Simulations . . . 10
- 2.2 Sink Particles . . . 11
- 2.3 Supersonic Turbulence . . . 12

3 Simulations **13**

4 Results **16**
- 4.1 Sérsic Profil . . . 17
- 4.2 Orbital Circularity . . . 20
- 4.3 SMBH Analysis . . . 21

5 Conclusion **24**

Appendices **25**
- The Impact of Parameters . . . 26

Bibliography **30**

Chapter 1

Theory

This chapter will discuss some theoretical concepts in galaxy formation. First, we will begin with a brief history of how galaxies came to be, starting at the Big Bang. Later, we will look at a more in-depth analysis of supermassive black hole formation and accretion, as well as some turbulence effects.

1.1 An Overview of Galaxy Formation

When pointing a telescope at the night sky and looking as far back as possible, astrophysicists are met with the cosmic microwave background. This was first discovered by A. A. Penzias and R.W.Wilson in 1965, for which they received a Nobel Prize (Penzias and Wilson 1965). Throughout the years, more and more experiments have been conducted and a clearer image of the CMB could be established. A characteristic of this background radiation is its small thermal fluctuations. These are very important for the further evolution of the universe since perfectly uniform and isotropic initial conditions would not lead to any structure formations. It is widely accepted that these irregularities are due to quantum fluctuations up to 10^{-33} seconds after the Big Bang. These impurities were then magnified by the rapid inflation epoch.

Having a significant density fluctuation then leads to the denser parts of space having a stronger gravitational field than the less dense parts. This perturbation causes gravitational instability, the rate of which is dependant on the chosen cosmological model. At first these dense regions collapse less rapidly than the universe expands, but once a certain threshold is reached the compact regions start collapsing in on themselves. This leaves us with a dark halo consisting of dark matter and baryonic gas.

Another important mechanism in the evolution of galaxies is the way gas cools. One way that gas can lose heat is through radiative cooling, the type of which is dependent on the virial temperature of the gas inside the dark matter halo. For high virial temperatures ($T_{\rm vir} \geq 10^7$K), the gas will mostly cool through bremsstrahlung. At lower temperatures, (10^4K$< T_{\rm vir} < 10^6$K) cooling occurs through a process called collisional ionisation. Here particles collide and then decay radioactively into their ground state. At even lower temperatures cooling can only happen if there are enough hydrogen atoms present. When forming molecular hydrogen, energy is released in the form of radiation which cools the gas.

$$\mathrm{H}^0 + e \rightarrow \mathrm{H}^- + \gamma \quad \text{and} \quad \mathrm{H}^- + \mathrm{H}^0 \rightarrow \mathrm{H}_2 + e \tag{1.1}$$

Another mechanism is Compton cooling, where low-energy photons pass through the gas and interact with the electrons. Through Compton scattering, the photons exchange energy

with the electrons and, if the energy of the photons is lower than that of the electrons, cooling occurs.

As cooling takes place, the self-gravity of the gas inside the dark matter halo starts to dominate. This leads to the gas starting to collapse in on itself, which in turn increases its density and temperature. If the cooling rate increases faster than the rate of collapse, runaway collapse is inevitable. This will cause the formation of numerous high-density cores, which will eventually form stars. It needs to be noted, though, that this process of star formation is not very well understood.

From this very brief overview it can be concluded that, in the end, the galaxy is mostly made up of cold gas and stars. Observations, however, tell us that this is not the case. The reason for that is that feedback processes have not yet been taken into consideration. We will study the feedback process of supermassive black holes in the following section. (Mo, Bosch, and White 2010)

1.2 Galaxy Morphology

The first-ever classifications of galaxies were done by Hubble. He arranged them in what is now known as a 'tuning fork' diagram (Hubble 1926) (Figure 1.1), the name of which arising from its characteristic shape.

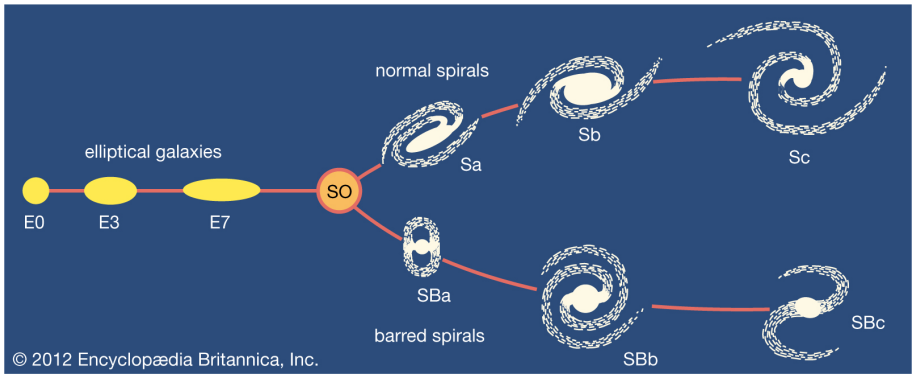


Figure 1.1: Hubbel 'tuning fork' sequence (Encyclopædia Britannica 2012)

1.2.1 Elliptical Galaxies

The elliptical galaxies are depicted on the left side of the image. Such galaxies are sometimes also referred to as 'early type' galaxies since they seem to have formed early on in the evolution of the universe. Hubble denoted them with the letter E followed by a number between 0 and 7 which signalises how elongated the galaxy is. This can be calculated through its ellipticity or 'flattening' (Binney and Scott Tremaine 2008, Chapter 1).

$$\epsilon \equiv 1 - \frac{b}{a} = \frac{n}{10} \tag{1.2}$$

Here n is the integer to define the galaxy and b/a is the axis ratio. Such galaxies are thought to be devoid of cool gas and show little sign of current star formation. When looking at their appearance they seem to show almost no visible structure or edge but rather fade into nothingness. Another characteristic of the elliptical galaxies is their surface brightness, which can be described by the Sérsic profile (Sérsic 1963).

$$I(R) = I_e \exp\left\{-b_n[(R/R_e)^{1/n} - 1]\right\} \tag{1.3}$$

The effective radius R_e is the radius of the isophote (contour of constant surface brightness) containing half of the total surface luminosity. Similarly, the effective luminosity I_e is the luminosity at R_e. The most important part of this equation is the Sérsic index n, which for elliptical galaxies, ranges from 2 for dim, to 6 for bright galaxies. A Sérsic index of $n = 4$ would reproduce de Vaucouleurs' law for elliptical galaxies (de Vaucouleurs 1948). The pre-factor b_n in the exponent can be approximated to be $b_n \approx 2n - 0.324$ as long as $n > 1$.

1.2.2 Spiral Galaxies

The two right arms of the Hubble sequence show the spiral galaxies, with spiral arms ranging from tightly to loosely bound. On top, the normal spirals are shown and on the bottom the barred ones. The difference lies in the origin of the spiral arms. In normal spirals, the characteristic spiral arms emerge directly from the nucleus of the galaxy whereas, in barred ones, there is a bar pierced through the nucleus from which the spiral arms emerge. Normal or barred, spiral galaxies are composed of a disk and a bulge at the centre. The bulge is commonly also described by a Sérsic profile and $n = 1$ usually is a good fit.

1.2.3 Lenticular Galaxies

At the fork of the Hubble sequence lie the lenticular galaxies. They indicate a cross-over between spiral and elliptical galaxies, contain a disk and a bulge, and follow a similar Sérsic profile as spiral galaxies. On the other hand, they mirror elliptical galaxies in their lack of cool gas and star formation activity and do not show any evidence of spiral arms. Hence they are placed in their own category.

1.3 Supermassive Black Holes

At the centre of most galaxies lies an active galactic nucleus (AGN) which is driven by a SMBH black hole with a mass of $M = 10^6 - 10^9$ $\mathrm{M}_\odot$. From a general relativity perspective, a black holes is nothing more than a region of space that has a certain geomerty. They way space-time bends and curves in the presence of matter was first described by Einstein's field equation more than 100 years ago in 1915.

$$G_{ij} - \Lambda g_{ij} = \frac{8\pi G}{c^4} T_{ij} \tag{1.4}$$

For an observer in a vacuum, outside a spherically symmetric matter distribution and for $\Lambda = 0$, the solution to this equation is the Schwarzschild metric.

$$ds^2 = c^2 \left(1 - \frac{2GM}{rc^2}\right) dt^2 - \left(1 - \frac{2GM}{rc^2}\right)^{-1} dr^2 - r^2 d\vartheta^2 - r^2 \sin^2 \vartheta d\varphi^2 \tag{1.5}$$

It isn't hard to see that at $r = 2GM/c^2$ the solution diverges, defining the event horizon of a black hole. More commonly, this radius is known as the Schwarzschild radius and describes the point after at which a body of mass becomes a black hole. As an example, the earth would have to be compressed to a ball of a few centimetres in diameter before it would form a black hole.

$$R_\mathrm{S} = \frac{2GM}{c^2} \tag{1.6}$$

1.3.1 Formation

Similar to star formation, also black hole formation is not well understood. Nevertheless, there are multiple hypotheses, one of them being that the first massive black holes formed from early-type stars called population III stars (Swinburne University of Technology 2021). Such stars are almost entirely composed of hydrogen and helium and hence are extremely metal-poor. These stars are also thought to have masses ranging from 100 $M_\odot$ to 300 $M_\odot$. If such a star has a mass above 250 $M_\odot$, then the internal silicon and oxygen burning is not enough to make the star explode at the end of its lifetime and it will directly collapse into a massive black hole (Fryer, Woosley, and Heger 2001). After its formation, it continues to grow by accreting material.

Another hypothesis is that black holes formed through the direct collapse of dense gas. This becomes the case if there is enough gas that does not cool below a threshold of 10^4K. Then it can collapse directly into a black hole (Montero, Janka, and Müller 2012), with its resulting mass being somewhere in the range of $10^4 - 10^5$ $M_\odot$ (Bromm and Loeb 2003).

1.3.2 Accretion

Naturally, many different physical processes need to be taken into account when describing the accretion of mass onto a black hole. Here only a very simple picture will be regarded where a particle is moving towards a black hole with a certain velocity v and distance r to the massive object (Shu 1991). The point where the kinetic energy and the gravitational potential energy are equal is where the particle becomes bound.

$$\frac{1}{2}mv^2 = m\frac{GM_\bullet}{r} \tag{1.7}$$

From this the Bondi radius r_B can be found which marks the distance after which the particle falls onto the body and gets accreted.

$$r_B = \frac{2GM_\bullet}{v^2} \tag{1.8}$$

The amount of mass ΔM that the black hole accretes in a given time-step Δt is $\Delta M = \rho v r_B^2 \pi \Delta t$ which gives us the accretion rate $\dot{M}_{\text{acc}}$.

$$\dot{M}_{acc} = \rho v \pi r_B^2 = \rho \frac{(2GM_\bullet)^2}{v^3} \tag{1.9}$$

The velocity v of the accreted material can be taken as the sum of the sound speed and the bulk velocity $v^2 = c_s^2 + v_{\text{bulk}}^2$. Since the sound speed will depend on the temperature in a given region, it is assumed that the particles' velocities follow a Maxwell-Boltzmann distribution $c_s^2 = \frac{k_b T}{m_p}$.
This accretion will not go on forever but will be stopped once a certain threshold is reached. At some point, the radiative pressure of the black hole accretion disk will become larger than the gravitational pressure which will inevitably halt accretion. Setting the gravitational and radiative forces equal produces a maximal luminosity (Mo, Bosch, and White 2010):

$$\frac{GM_\bullet}{r^2}\rho = \sigma_T \frac{L}{4\pi r^2 c} n_e \longrightarrow L_{\text{edd}} = \frac{4\pi c m_p G M_\bullet}{\sigma_T} \tag{1.10}$$

Here L_{edd} is the Eddington luminosity and can be related to a maximal accretion rate $\dot{M}_{\text{edd}}$, where ε_r the radiative efficiency. Finally, accretion will come to a halt once its rate has exceeded the Eddington accretion rate:

$$\dot{M}_{\text{edd}} = \frac{L_{\text{edd}}}{\varepsilon_r c^2} \tag{1.11}$$

1.3.3 Active Galactic Nuclei and Feedback

Other than the rest of the galaxy, the AGN emits radiation ranging from radio to gamma-rays. This radiation is created by the supermassive black hole's gravitational energy in a process called feedback. Here, energy is released into the gas of the galaxy either through radiative or mechanical processes. We have already discussed the radiative feedback in the previous section where we found that the luminosity is proportional to the accretion rate of the black hole:

$$\frac{dE}{dt} = \varepsilon_r \dot{M}_\bullet c^2 \tag{1.12}$$

For bright active galactic nuclei, the accretion efficiency can range from 0.1-0.2 (Yu and S. Tremaine 2002). When the accretion rate is a lot lower the feedback process acts mechanically, through radio jets for example.
The fact that the AGN feedback pushes energy into the interstellar medium can lead affected gas to have enough energy to leave the galaxy. This can largely impact the star formation rate, which is tightly correlated to the amount of gas available.

Chapter 2

Computational Techniques

To learn more about the way galaxies, stars, and other astrophysical bodies form and behave, astrophysicists are turning more and more to computational methods. Due to the high complexity of these systems, it is nearly impossible to test a hypothesis without running a simulation on a high-power computer. Such simulations would then be compared to observational data and tweaked where necessary.

2.1 Ramses

The simulations in this thesis were done with the N-body and hydrodynamical code Ramses (R. Teyssier 2002). Since the code was first presented it has continually been modified and as of now, it has proven to be useful for the simulation of galaxy formation and evolution. All this while taking into consideration not only gravity and hydrodynamics but also feedback mechanisms, AGN and magnetohydrodynamics as well as heating and cooling. I will briefly introduce two key ingredients of the Ramses code: the Adaptive Mesh Refinement routine which characterises the grid of the simulation and the hydrodynamical solver.

2.1.1 Hydrodynamics with Adaptive Mesh Refinement

Rather than tracking individual particles, the Ramses code works with a grid where each cell contains some physical properties (mass density, temperature, etc.). To calculate the forces and interactions between the cells accurately, each cell must have a similar resolution. This is impossible with a static grid and hence Ramses instead uses an adaptive mesh refinement routine. The data structure used is a "Fully Threaded Tree" (Khokhlov 1998) in which each cell can have up to 2^{dim} children cells, called *octs*. In three dimensions one would have a tree that goes eight levels deep, as shown in Figure 2.1. When linking data between children cells, instead of having to go all the way up and down the tree the cells are linked between each other. In 3 dimensions each oct at level ℓ has a pointer to its neighbouring octs as well as to its parent cell and neighbouring parent cells at level $\ell - 1$. It also has a link to its children cells a level down at $\ell + 1$.

The program is given some threshold after which a cell needs to be refined, such as a mass density or temperature, and repeatedly checks the cells for these conditions starting at the finest level. If a cell meets the given conditions then it will be marked for refinement. It will also be marked for refinement if it contains one or more children cells that are already refined. In a second run through it will either remove children cells from a non-marked parent cell or create children cells for a child cell which is marked for refinement.

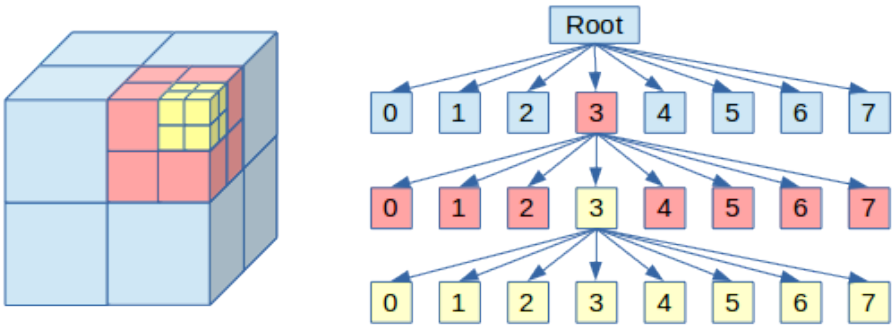


Figure 2.1: Visualisation of the first three levels of an octree (The Infinite Loop 2014)

Ramses takes into consideration both collisionless particles, such as dark matter, and collisional particles such as baryons. In order to describe compressible and inviscid fluids, such as astrophysical gas, the Euler equations need to be solved.

$$\frac{\partial \rho}{\partial t} + \nabla \cdot (\rho \mathbf{v}) = 0 \tag{2.1}$$

$$\frac{\partial}{\partial t}(\rho \mathbf{v}) + \nabla \cdot (\rho \mathbf{v} \otimes \mathbf{v}) + \nabla p = -\rho \nabla \varphi \tag{2.2}$$

$$\frac{\partial}{\partial t}(\rho e) + \nabla \cdot [\rho \mathbf{v}(e + p/\rho)] = -\rho \mathbf{v} \nabla \varphi \tag{2.3}$$

Here ρ, $\mathbf{v}$, φ and e are the mass density, velocity, gravitational potential and specific total energy. The thermal pressure p can also be written as

$$p = (\gamma - 1)\rho \left(e - \frac{1}{2} u^2 \right) \tag{2.4}$$

where γ is the adiabatic index. Choosing $\mathbf{U} = (\rho, \rho\mathbf{v}, \rho e)$ to be the state vector, $\mathbf{F} = (\rho\mathbf{v}, \rho\mathbf{v} \otimes \mathbf{v} + p, \rho\mathbf{v}(e + p/\rho))$ to be the flux term and $\mathbf{S}$ to be the source term, the Euler equations can be written as:

$$\frac{\partial \mathbf{U}}{\partial t} + \nabla \mathbf{F} = \mathbf{S} \tag{2.5}$$

or in a discretised version

$$\frac{U_i^{n+1} - U_i^n}{\Delta t} + \frac{F_{i+1/2}^{n+1/2} - F_{i-1/2}^{n+1/2}}{\Delta x} = S_i^{n+1/2} \tag{2.6}$$

where U_i^n is the the numerical approximation of $\mathbf{U}$ at time t^n for cell i. Since gravity here is treaded as a *non-stiff* (meaning the numerical methods will not make the solution numerically unstable), it is possible to solve the Euler equations part by part, by using the operator splitting method. The source term will be computed by using a fractional step method. Then the flux terms in the conservative Euler equation are found using a second-order Godunov method. A step-by-step run-through of how this is then implemented in the AMR steps is given in R. Teyssier 2002.

2.1.2 Cosmological Simulations

Cosmological simulations are frequently used to test cosmological models, the one most consistent with observations is the concordance model or the ΛCDM model. When wanting to study smaller structures, such as galaxy clusters, or even singular galaxies, it becomes

incredibly expensive to simulate such a large box-size (usually within $10 - 100$ Mpc h^{-1}) with large enough resolution to see the structures of a given galaxy. Due to this, zoom-in cosmological simulations are often used instead. Here, a large 'box' of the universe is first simulated on a coarse level for a certain cosmological model and initial conditions. Once completed, a target dark matter halo is selected and new initial conditions are generated for a smaller box (usually with box-length 0.001 times smaller) encapsulating the halo. This dark matter halo is then re-simulated on a finer level and with the new initial conditions. In Ramses, the cosmological simulations can be turned on by denoting `cosmo=.true.` in the `&RUN-PARAMS` section of the namelist file. Specific parameters for the cosmological run can also be found in the file `cosmo.nml`, which is located in the namelist folder of the Ramses code.

2.2 Sink Particles

Sink particles are used to simulate dense objects which are a lot smaller than the resolution of the grid. First used in smoothed particle hydrodynamical codes (Bate, Bonnell, and Price 1995), they are now also implemented in the Ramses code to simulate black holes. A few years ago the sink particle implementation in Ramses was refurbished and now uses a clump finder (Bleuler and Teyssier 2014). First, the clump finder finds all density peaks within the system and assigns an id to them. Subsequently, it will also check for saddle points above a certain threshold. If the peak-to-saddle point ratio is below a certain value then the peak is not deemed sustainable and its id will be merged with the neighbouring peaks id connected by the saddle. All this is done on the fly with the PHEW algorithm (A. Bleuler et al. 2015).

Sink formation sites are also determined by the clump finder and later on checked for gravitational instability. If the gas in such a formation region is contracting along all axes at a certain rate, then it is deemed to be collapsing into a sink particle. It also needs to be checked if the gravitational field of the contracting gas is able to overcome the thermal energy of the gas. The region will also be scanned for pre-existing sink particles. This will prevent gas that is being accreted onto a sink particle to be misinterpreted as a newly forming sink particle.

After the sink particle is created, it will be assigned an initial mass, usually around 10^5 $M_\odot$. Its mass will then be distributed onto particles, which each lie half a grid spacing apart, using the cloud-in-cell scheme. These particles are then placed onto a sphere and used to calculate the trajectory of the sink, with the sinks acceleration being equal to the average of all the particles' accelerations.

Sinks can gain mass in two ways: either through accretion or through merging. In the Ramses code, sink merging is a mechanism that can be turned off and on. If enabled, then two sinks will merge if they are at a certain distance from each other. Accretion, on the other hand, is calculated using the Bondi-Hoyle-Lyttleton accretion rate which was discussed earlier on. If the accretion rate exceeds the Eddington limit then it will come to a halt. Numerically, after accreting gas, the sink particles' mass, position, velocity, and angular momentum need to be updated. This is done by using the old values of the sink particle as well as the mass and angular momentum which was removed from the gas.

$$M_s^{\text{new}} = M_s^{\text{old}} + \sum_{i \in \text{cells}} \Delta m_i \tag{2.7}$$

$$\boldsymbol{R}_s^{\text{new}} = \frac{1}{M_s^{\text{new}}} \left(\boldsymbol{R}_s^{\text{old}} M_s^{\text{old}} + \sum_{i \in \text{cells}} \boldsymbol{r}_i \Delta m_i \right) \tag{2.8}$$

$$\boldsymbol{V}_s^{\text{new}} = \frac{1}{M_s^{\text{new}}} \left(\boldsymbol{V}_s^{\text{old}} M_s^{\text{old}} + \sum_{i \in \text{cells}} \boldsymbol{v}_i \Delta m_i \right) \tag{2.9}$$

$$\begin{aligned} \boldsymbol{L}_s^{\text{new}} = & \boldsymbol{L}_s^{\text{old}} + (\boldsymbol{R}_s^{\text{new}} - \boldsymbol{R}_s^{\text{old}}) \otimes (\boldsymbol{V}_s^{\text{new}} - \boldsymbol{V}_s^{\text{old}}) M_s^{\text{old}} \\ & + \sum_{i \in \text{cells}} (\boldsymbol{R}_s^{\text{new}} - \boldsymbol{r}_i) \otimes (\boldsymbol{V}_s^{\text{new}} - \boldsymbol{v}_i) \Delta m_i \end{aligned} \tag{2.10}$$

2.3 Supersonic Turbulence

The simulations in this thesis were carried out with supersonic turbulence implemented (Kretschmer and Romain Teyssier 2019). Doing so requires using an appropriate sub-grid scale model and solving the turbulent kinetic energy equation:

$$\frac{\partial K_T}{\partial t} + \nabla(K_T \mathbf{v}) + P_T \nabla \mathbf{v} = S_T - D_T \tag{2.11}$$

Here K_T is the turbulent kinetic energy and the turbulent pressure $P_T = \frac{3}{2} K_T = \bar{\rho} \sigma_{1D}^2$. σ_{1D} is the 1D turbulent velocity dispersion and is proportional to the 3D turbulent velocity dispersion $\sigma_{3D} = \sqrt{3}\sigma_{1D}$, which will become important in the next chapter.
On the right side of the equation, we have S_T as the so-called creation term and D_T as the destruction term. The destruction term can also be seen as the turbulent kinetic energy divided by the dissipation time.

$$D_T = \frac{K_T}{\tau_{\text{diss}}} \quad \text{with} \quad \tau_{\text{diss}} = \frac{\Delta x}{\sigma_{1D}} \tag{2.12}$$

The creation term, on the other hand, models the turbulent kinetic energy through shear flows. It is directly proportional to the turbulent viscosity parameter μ_T with $\widetilde{S}_{ij}$ being the shear tensor:

$$S_T = \frac{1}{2} \mu_T |\widetilde{S}_{ij}|^2 \quad \text{with} \quad \bar{\rho} \Delta x \sigma_{1D} \tag{2.13}$$

Here we run into an issue since shear flows are not necessarily always turbulent under the influence of gravity. Hence this model might be overestimating turbulence. Furthermore, it might also be underestimating it since a gravitationally unstable disk could create even more turbulence. Nevertheless, I will be using the turbulent velocity dispersion σ_T later on to more accurately simulate the matter accretion onto supermassive black holes.

Chapter 3

Simulations

In this thesis, four simulations were performed with the same initial conditions. Since the goal is to probe the impact of SBMH on galaxy morphology, it was important that these simulations only differ minimally. Thus the only parameters differentiating them are the sink particles and turbulence during sink accretion. The former is a run parameter whereas the latter needed to be patched into the code.

	Sink particles	Turbulent accretion
1	False	-
2	True	False
3	True	True

Table 3.1: Configurations for the three different simulations.

Implementing turbulence into the accretion of matter onto sink particles consisted of adding an energy term to the thermal energy. The goal of this is to make the Bondi velocity more realistic by adding the turbulent velocity dispersion σ_T to it.

$$v_{\text{eff}}^2 = c_s^2 + v_{\text{bulk}}^2 + \sigma_T^2 \tag{3.1}$$

$$\dot{M}_{\text{Bondi}} = 4\pi\rho\frac{GM_\bullet}{v_{\text{eff}}^3} \tag{3.2}$$

The implementation of this was done in the subroutine `collect-acczone-avg-np` of the sink particle file in the RAMSES code.

```
! Compute sink average quantities
wvol(isink)=wvol(isink)+weight
wden(isink)=wden(isink)+weight*d
wmom(isink,1:ndim)=wmom(isink,1:ndim)+weight*d*vv(1:ndim)
weth(isink)=weth(isink)+weight*d*e+uold(indp(j,ind),ivirial1)*weight
```

In the last line, the weighted turbulent kinetic energy was added to the weighted thermal energy. This was then patched into the RAMSES code for the simulations with turbulence implemented into the sink accretion.
To run the code there also needed to be a set of initial conditions available which in

Ramses are generated by the algorithm Music (Hahn and Abel 2011). Music (MUlti-Scale Initial Conditions) is made for generating cosmological initial conditions for "zoom-in" simulations. Besides the initial conditions, there also are numerous parameters that need to be set before starting the run such as the global properties, initial conditions, AMR grip properties, and data output. One can also define conditions for processes such as star formation, clump-finder, or feedback mechanisms. I will now briefly describe the conditions chosen for the sink particles:

```
&SINK_PARAMS
smbh=.true.
agn=.true.
create_sinks=.true.
nsinkmax=2000
mass_sink_direct_force=1.d3
ir_cloud=4
sink_soft=2
mass_sink_seed=1.d4
mass_smbh_seed=0
mass_halo_AGN=1.d7
mass_clump_AGN=1.d6
mass_star_AGN=1.d7
accretion_scheme='bondi'
eddington_limit=.true.
agn_acc_method='mass'
agn_inj_method='volume'
acc_sink_boost=-1
boost_threshold_density=0.1
bondi_use_vrel=.true.
verbose_AGN=.true.
AGN_fbk_mode_switch_threshold=-1
AGN_fbk_frac_ener=1.0
T2_min=0.
T2_AGN=0.15d12
AGN_fbk_frac_mom=0.0
epsilon_kin=0.1
kin_mass_loading=1.
cone_opening=20.
sink_descent=.true.
fudge_graddescent=1.0
/
```

The very first entry states that the implemented sink particles behave like supermassive black holes instead of stars. Those SMBH were then also chosen to be driving an active galactic nucleus, meaning they produce feedback. Another important parameter is the initial mass of the sink which was chosen to be 10^4 $M_\odot$. This was mostly motivated by the fact that the resulting mass of black holes created through a direct collapse is within the range of $10^4 - 10^5$ $M_\odot$ (Bromm and Loeb 2003). As mentioned previously, I am also considering the black hole accretion to be Bondi and to be stopped once the Eddington limit is reached. Both of these conditions were also set in the sink parameters. The last parameter adds some artificially fabricated drag to the sink particles. This is especially

helpful if you want your sinks to be able to merge. If set to zero the sink particles, even when getting really close to one another, seldom bind or merge but rather just dash past each other. Some of the parameters such as "AGN feedback switch mode threshold" were turned off since the simulations would simply take too long for the scope of this thesis. Four more simulations with different parameters were run which are described in the appendix. Once all the parameters were set it was time to start the simulations. After that, it was a pure waiting game combined with checking the log files once in a while to make sure everything was looking physical.

Chapter 4

Results

In this chapter, I would like to present the analysis done on the simulations and discuss their outcomes. Before taking a closer look at the analysis of the bulges of the galaxies, I will first examine the shape and morphology of the galaxies from a purely optical point of view.

In Figure 4.2 the evolutions of the galaxies in question are shown from their early stages at redshift $z = 3.0$ to today $z = 0.0$. At first glance, one can see a difference between the simulations with and without supermassive black holes.
The two galaxies of the simulations with sink particles at redshift $z = 0.0$ do not seem to exhibit much structure. Due to this, as well as the similarity between the face-on and side-on view, point towards them being elliptical galaxies. Distinguishing between the two simulations with SMBH's proves to be a bit harder just from Figure 4.2 and will be discussed later on.
The galaxy without sink particles has a far more peculiar shape. The central disk and its structure point more towards a spiral galaxy than an elliptical one, even though it doesn't show very defined spiral arms. It is too early to say at this point, but the lack of spiral arms could also indicate a lenticular galaxy. Apart from this, it also has a ring of dust almost perpendicular to the disk. Looking at its side-on view at redshift $z = 1.0$, it seems like a part of the disk was flung away and later formed a ring-like shape. Such warps in the disk of a galaxy are quite common but their origin is still a topic of research. When looking at Figure 4.1 one can see this ring structure also for the elliptical galaxies. Another surprising observation is that, for the galaxies with an active galactic nucleus, there is almost no gas left, which could be due to the SMBH feedback heating up the gas high enough for it to be able to leave the galaxy.

The matter contents of the galaxies can also be analysed by looking at the gas fraction of all baryonic mass within $0.1r_{\mathrm{vir}}$. One can also consider how high the baryon fraction is (within r_{vir}) in comparison to the average cosmic baryon fraction. In Table 4.1 one can see the values for the three simulations. The baryon fraction for the SMBH galaxies is a lot lower than the one without SMBH's. This is because in addition to the supernova-feedback the supermassive black holes also produce a significant amount of feedback, ridding the galaxy of a lot of gas. This can also be seen in the gas fraction which is significantly lower for the SMBH galaxies.

	f_{Gas}	f_{Baryon}
No SMBH	0.37	0.47
SMBH with turbulence	0.06	0.21
SMBH without turbulence	0.11	0.24

Table 4.1: The gas fraction and baryon fraction for the three simulations.

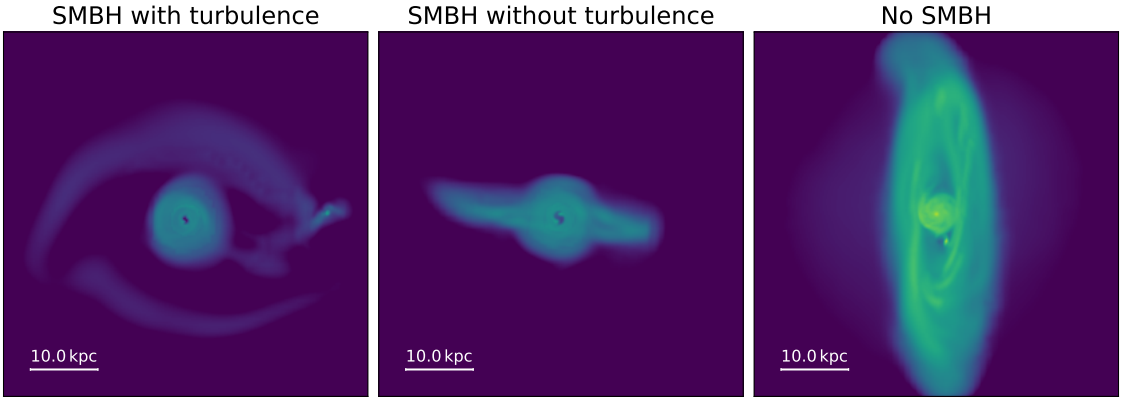


Figure 4.1: Above one can see the gas contents of the galaxies at redshift $z = 0$.

4.1 Sérsic Profil

To analyse the luminosity profile of the three galaxies, a Sérsic profile was fitted to them. First, the stellar mass of the galaxy was used to calculate its surface brightness distribution. This was done by splitting the galaxy up into donut-shaped rings with width Δr around the centre of the galaxy and effectively calculating the density profile $\Sigma(r) = m(r)/2\pi r\Delta r$. Even though this is not exactly the surface luminosity, it behaves similarly enough and thus was used as an analogy to it. After plotting that against the radius, it became clear that a single Sérsic fit would not suffice and a double Sérsic fit was used instead:

$$\begin{aligned} I(r) =& I_{0,\text{in}} \exp\left[-b_{n,\text{in}}\left(\left(\frac{r}{r_{e,\text{in}}}\right)^{1/n_{\text{in}}} - 1\right)\right] \\ &+ I_{0,\text{out}} \exp\left[-b_{n,\text{out}}\left(\left(\frac{r}{r_{e,\text{out}}}\right)^{1/n_{\text{out}}} - 1\right)\right] \end{aligned} \tag{4.1}$$

To not have too many free parameters, the outer regions were assumed to be equivalent to an exponential disk (Freeman 1970) and hence the Sérsic index n_{out} was set to be 1. This would allow us to use the inner Sérsic index n_{in} to describe the bulge of the galaxy. The three fits for the simulations at redshift $z = 0.0$ are shown in Figure 4.3 as well as some values in Table 4.2. Even though the "goodness" of the fit R^2 is below 95%, I still believe there are some conclusions that can be drawn from it. The Sérsic indices for the two simulations with sink particles implemented are within the range of possible indexes for elliptical galaxies, which agrees with their true colour renders. It is interesting to see the large difference between the galaxy with and without turbulent accretion. While the galaxy without turbulent accretion seems to be quite a dim elliptical, the galaxy with turbulent accretion perfectly fits De Vaucouleurs's law. On the other hand, the galaxy without sink particles has a very large Sérsic index for a spiral or lenticular galaxy.

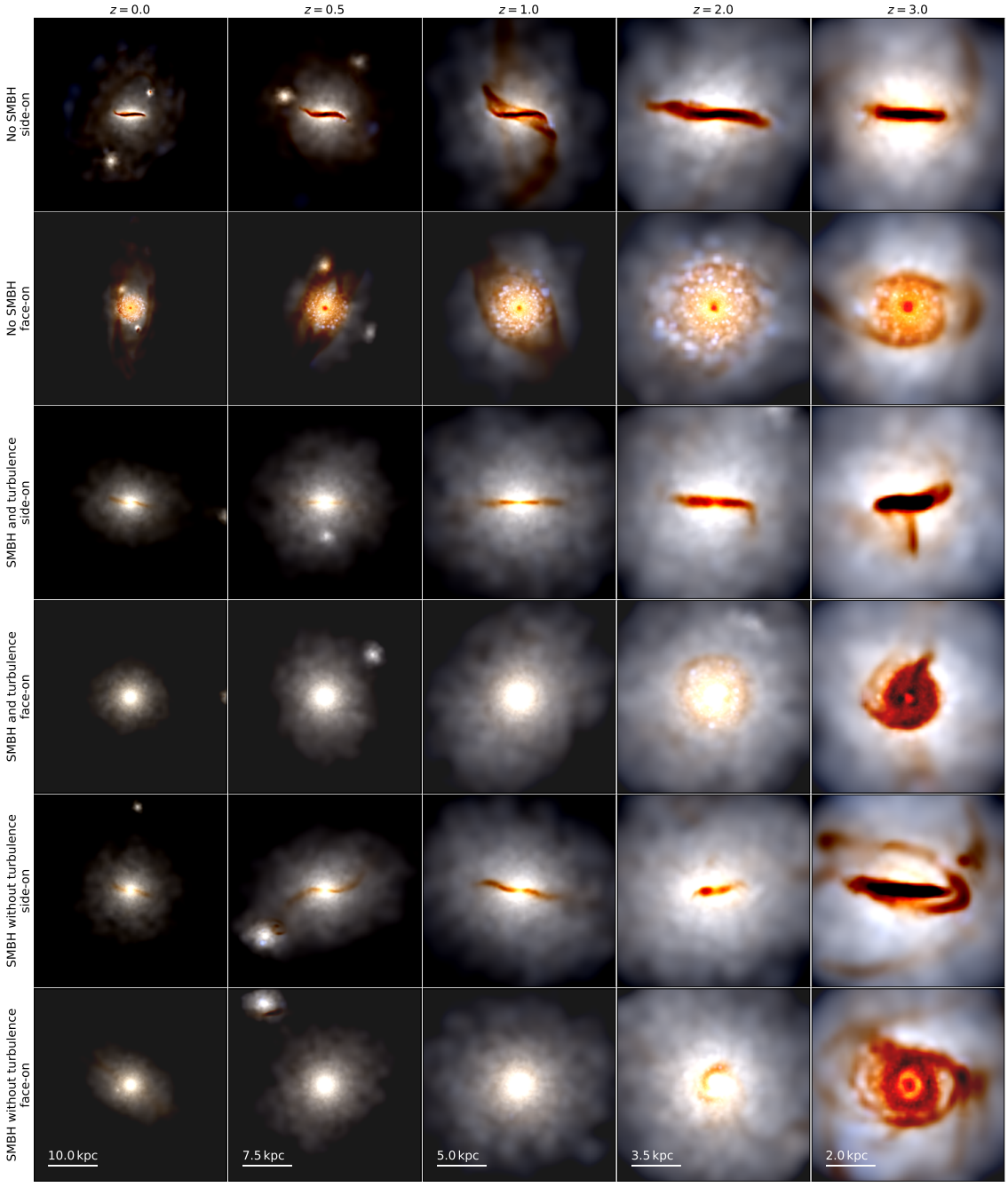


Figure 4.2: Above one can see a true colour render of the three simulations run. The two top rows are both the face-on and side-on view of the simulation without sinks and the lower four depict the simulations with sink particles and turbulence either turned on or off in accretion. From left to right redshift decreases from 3.0 to 0.0, allowing us to see the evolutions of the galaxy. Not only stars are depicted here but also light absorption of dust particles.

	n_{in}	R^2
No SMBH	3.7 ± 0.1	0.82
SMBH with turbulence	4.0 ± 0.1	0.87
SMBH without turbulence	2.5 ± 0.1	0.83

Table 4.2: Above both the inner Sérsic index n_{in} as well as the "goodness" of the fit R^2 are shown for the stellar mass in the three simulations.

It needs to be noted, however, that analysing these galaxies at slightly higher redshifts can change the Sérsic index dramatically, as shown in Figure 4.4. The values for n_{in} for the simulations with sink particles are extremely volatile between redshift $z = 0.5$ and $z = 0.0$. Nevertheless, the values still stay within the range of possibility for elliptical galaxies. On the other hand, the Sérsic index for the galaxy without a SMBH seems to be increasing quite steadily and after redshift $z = 2$ is quite large for a galaxy with a disk.

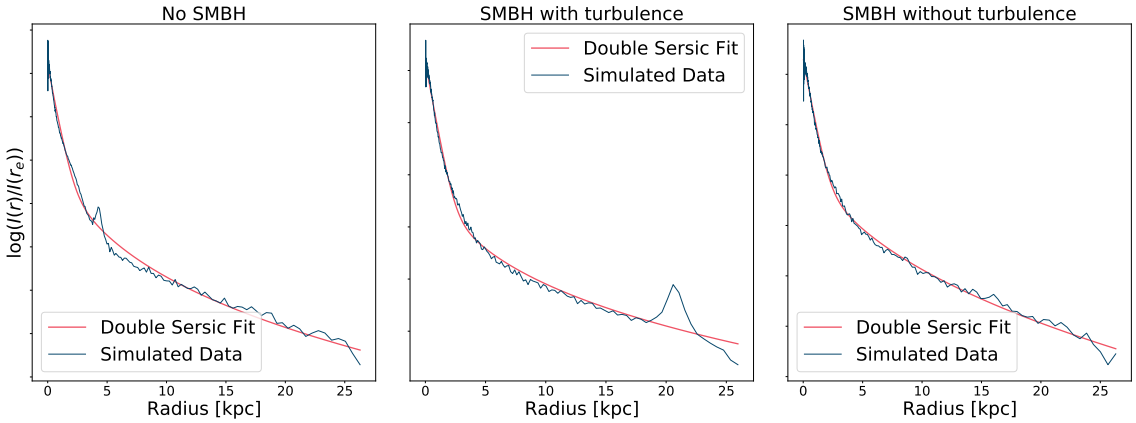


Figure 4.3: Here the surface density profiles of three galaxies in question are shown with their respective Sérsic fit. In this case only the luminosity from stars was considered and instead of a regular Sérsic profile a double Sérsic profile was used.

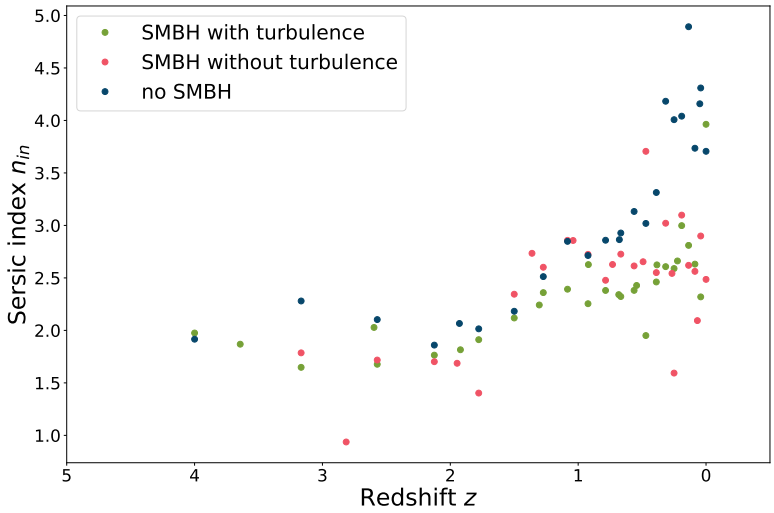


Figure 4.4: Displaying the Sérsic index over the lifetime of the galaxy shows that the values shown in Table 4.2 are not necessarily the whole story.

Cold Gas

We can also take a look at the gas contents of the galaxies. In order to find the surface brightness I only consider cold gas which is below a temperature of $5 \cdot 10^4$K. The reason I decided to only look at gas below a certain temperature, is because it is known that disks are made up of stars as well as cold gas. Ellipticals on the other hand show very little cold gas at all. In Figure 4.5 the Sérsic profiles are displayed. For the two galaxies with SMBH's one can see a second bump at about 8 kpc. I believe these bumps to be due to satellites which are visible in Figure 4.2 and 4.1. Hence, I did not include them in the Sérsic fit.
In Table 4.3 we can see that the Sérsic index for the SMBH galaxies is very low. This agrees with my previous hypothesis that the SMBH feedback rid the galaxy of its cold gas. Besides, this also corresponds to my belief that we are dealing with two elliptical galaxies since those are devoid of cold gas as well. Other than for the star mass, the Sérsic index for the cold gas of the non-SMBH galaxy agrees more with a disk-shaped galaxy since its value is close to one. It needs to be noted though that for these three fits the R^2 value is a lot lower and hence any analysis of it needs to be taken lightly.

	n	R^2
No SMBH	1.3 ± 0.4	0.24
SMBH with turbulence	0.3 ± 0.1	0.68
SMBH without turbulence	0.3 ± 0.1	0.13

Table 4.3: In this table both the Sérsic index n as well as the "goodness" of the fit R^2 are shown for cold gas in the three simulations.

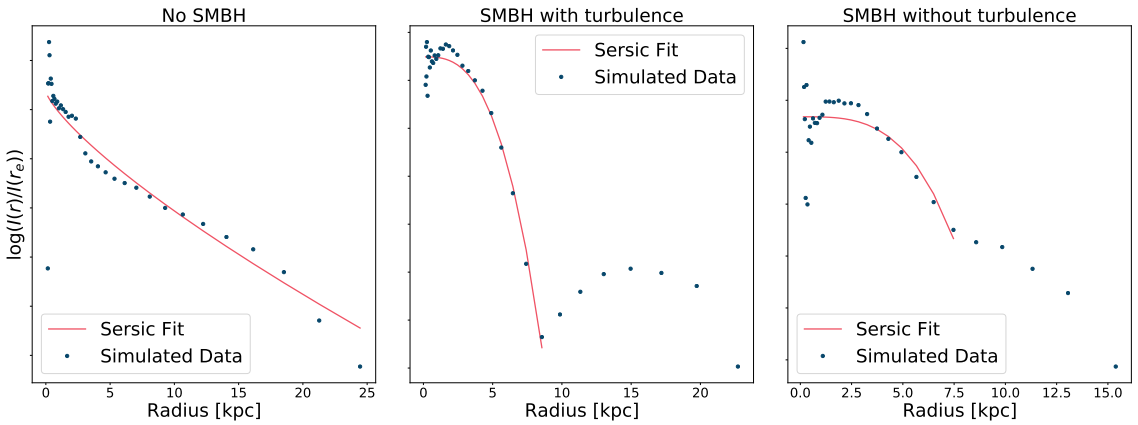


Figure 4.5: Above the surface density profiles of the gas contents of the three galaxies are shown. In addition a single Sérsic profile was fitted to the data.

4.2 Orbital Circularity

Another way to analyse a galaxy's morphology is by looking at the angular momentum of its star contents. The orbital circularity (Abadi et al. 2003) as

$$\epsilon = \frac{J_z}{J_{\text{circ}}(E)} \tag{4.2}$$

where $J_{\text{circ}}(E)$ is the maximal angular momentum for a given energy and J_z is the particles angular momentum component which is parallel to the angular momentum of the galaxy.

This fraction then gives us an insight into how much of the stellar mass is moving with or against the galaxy. A value of $\epsilon = 1$ means the star is moving on a circular orbit about the galaxy, or in other words, the star is located in the galactic disk. On the other hand $\epsilon = 0$ means the star is moving on a radial orbit and is located in the bulge.
In Figure 4.6 one can see a histogram of the circularity of the gas and stellar content for all three simulations. The dotted line denotes where I chose to set the crossover between the disk and the bulge. Dividing the bins below $\epsilon = 0.5$ by the ones above gives us a bulge to disk ratio, the values for which are shown in Table 4.4. Here once again the simulation without SMBH's stands out. A clear disk behaviour can be observed due to the sharp peak around $\epsilon = 1$. The second peak at $\epsilon = 1$ is a lot smaller but wider which leads to the bulge to disk ratio being close to 1. This once again shows us that the non-SMBH galaxy has a very large bulge for it being a non-elliptical galaxy.

When comparing the two SMBH-galaxies to each other, one can see a sharper peak at $\epsilon = 0$ for the SMBH without turbulent accretion simulation. This also leads to its bulge to disk ratio being higher than for the simulation with turbulent accretion. Nevertheless, both of these distributions are characteristic of elliptical galaxies.

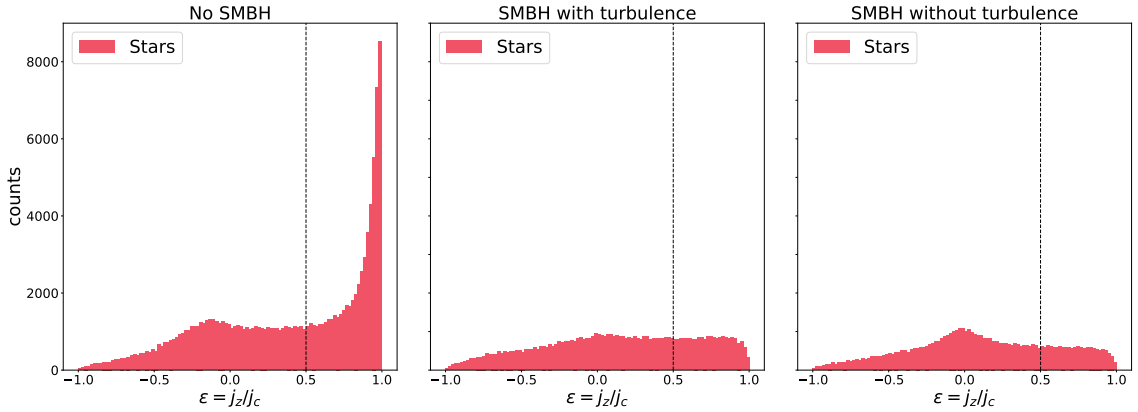


Figure 4.6: Here a histogram of the circularity of the three simulations at $z = 0$ is displayed.

	Bulge/Disk	$M_{\star,Gal}/M_\odot$
No SMBH	1.0	$2.6{\cdot}10^{10}$
SMBH with turbulence	2.4	$1.4{\cdot}10^{10}$
SMBH without turbulence	3.1	$1.2{\cdot}10^{10}$

Table 4.4: The bulge to disk ratio of the stellar contents of the three simulations as well as the total stellar mass within the galaxy is displayed above.

4.3 SMBH Analysis

This section will take a closer look at the supermassive black holes at the centre of two of the galaxies. In Figure 4.7 one can see both the accretion rate as well as the mass of the SMBH over time. Although both supermassive black holes level out at about the same mass we can see a delayed accretion for the SMBH with turbulence. Comparing this data to the Sérsic indices for the stellar mass of the two galaxies gives us a hint. It seems like the delay in accretion allowed for more star formation which in turn made the galaxy brighter. On the other hand, the SMBH in the galaxy without turbulence accreted mass too quickly, ridding the galaxy of its cold mass before it could form more stars.

It is also interesting to compare this to the renders in Figure 4.2. From the plot, it can be seen that the SMBH starts accreting mass at $z = 4$ and reaches its maximum mass at about redshift $z = 2.3$. In the render at redshifts $z = 3.0$, you can see a disk that at $z = 2.0$ starts to dissipate due to the SMBH feedback. On the other hand, the galaxy without a SMBH stays on its trajectory and becomes a disky galaxy.

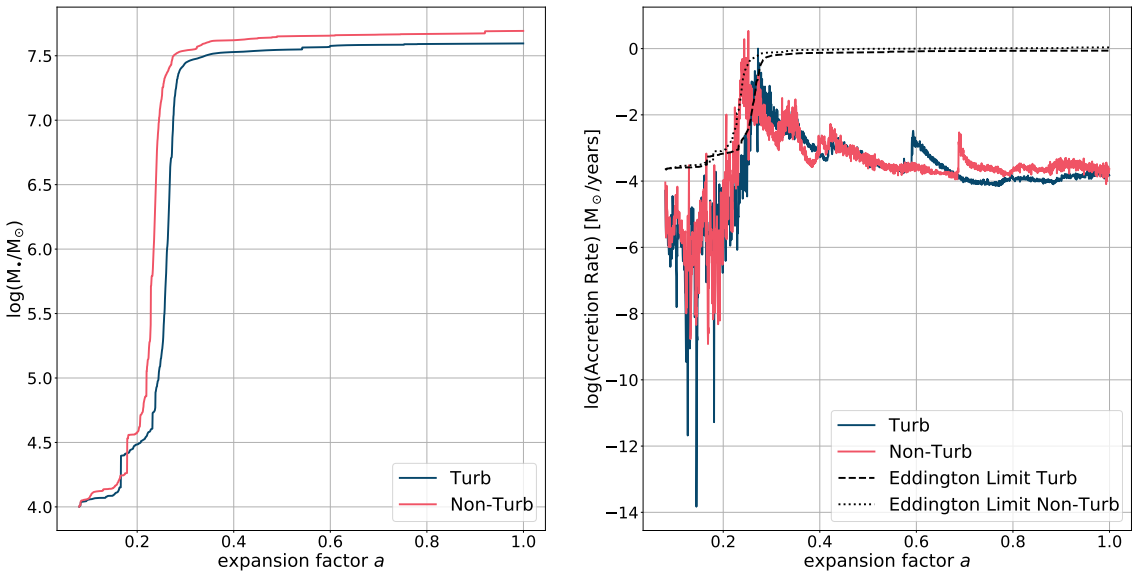


Figure 4.7: In this table one can see the accretion rate and mass of the SMBH at the centre of the galaxy as a function of the expansion factor a.

There is also a tight correlation between the black hole mass and the galaxy mass as well as the spheroid mass (Häring and Rix 2004). To determine the spheroid mass of the galaxies, its radius first needs to be defined. For this $r_{e,\mathrm{in}}$ from the double Sérsic fits was chosen to define where the bulk ends. Similarly, for the stellar galactic mass, I considered everything within $0.1 \cdot r_{\mathrm{vir}}$. In Table 4.5 the value for the black holes, stellar spheroid, and stellar galaxy mass are shown. A paper by Sahu, Graham, and Davis 2019 took a sample of early-type galaxies with either a Sérsic or core-Sérsic light profile and tested the correlation between their black hole mass and the stellar spheroid and galaxy mass. Performing a BCES bisector regression they found for the Sérsic galaxies that $M_{\mathrm{BH}} \propto M_{\star,\mathrm{sph}}^{1.38\pm0.21}$ and $M_{\mathrm{BH}} \propto M_{\star,\mathrm{gal}}^{1.61\pm0.18}$. Similarly for the core-Sérsic galaxies they found $M_{\mathrm{BH}} \propto M_{\star,\mathrm{sph}}^{1.30\pm0.14}$ and $M_{\mathrm{BH}} \propto M_{\star,\mathrm{gal}}^{1.47\pm0.18}$. Comparing my results to theirs in Figure 4.8, we can see that for the stellar spheroid the two simulations lie within one standard deviation of the Sérsic and Core-Sérsic fits. Also for the stellar galaxy mass, the data points are still within the error of the core-Sérsic fits. The fact that the data points seem to fit a core-Sérsic model more is not surprising, since earlier on I also decided to use a double Sérsic fit instead of a single one.

	$r_{e,\mathrm{in}}$ [kpc]	$\log_{10}(\mathrm{M_{BH}/M_\odot})$	$\log_{10}(\mathrm{M_{\star,sph}/M_\odot})$	$\log_{10}(\mathrm{M_{\star,gal}/M_\odot})$
$\mathrm{SMBH_{turb}}$	6.6	7.6	10.15	10.15
$\mathrm{SMBH_{no\ turb}}$	4.1	7.7	10.07	10.07

Table 4.5: Above logarithm of the black holes mass, stellar spheroid mass as well as stellar galaxy mass for the two simulations are shown. The value for the spheroid mass was calculated by adding all the stellar mass within $r_{e,\mathrm{in}}$.

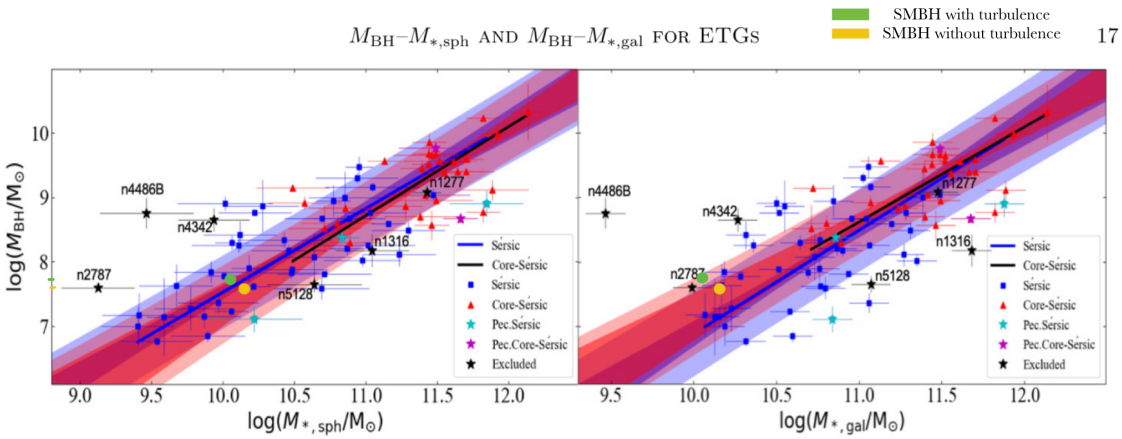


Figure 4.8: Above a figure from the research of Sahu, Graham, and Davis 2019 is shown. The dark blue and red lines represent the uncertainty $\pm\sigma$ on the slope and intercept of the lines where as the light blue and red lines show the $\pm\sigma$ rms data scatter about the blue and black regression lines. The data from my simulations has been drawn on in yellow and green (the data for which can be seen in Table 4.5).

Chapter 5

Conclusion

In this thesis, three cosmological simulations were performed with the adaptive mesh refinement hydrodynamical code Ramses. The goal was to compare the galaxy without an AGN to the ones with. By looking at the true colour renders of the galaxies in question, it was found that the galaxies with an active galactic nucleus resembled the shape of an elliptical galaxy. On the other hand, the galaxy without a SMBH showed a clear disk structure. Due to the resolution of the render, it is unclear whether this galaxy belongs into the spiral- or lenticular category. Further analysing the light profile of the samples with a Sérsic (and double Sérsic) fit, showed that the galaxy with no SMBH had an uncharacteristically large bulge. This issue was found over all redshifts. The galaxies with a SMBH showed a similarly large Sérsic index which, on the other hand, is what could be expected from an elliptical galaxy. Furthermore, the bulge-to-disk ratio of the stellar mass was tested by analysing the circularity of the galaxies. The non-SMBH galaxy showed a clear distinction between its disk and bulge, with them being about equally sized. A more spheroidal shape was seen for the circularity of the SMBH galaxies, with their bulge-to-disk ratio being well above one.

In a second step, the two galaxies with a SMBH were compared. Here the goal was to determine how implementing turbulence into the sink accretion changes the galaxy's morphology. By studying the mass of the two supermassive black holes at the centre of the galaxies over different redshifts, one could tell that turbulence seems to delay the SMBH accretion slightly. This is also reflected in the light profiles of the galaxies since for the simulation without turbulence, the galaxy is less bright. By delaying the mass accretion, the cold gas in the galaxy has more time to form stars before the SMBH becomes large enough for feedback to blow away all the remaining cold gas. The mass of a supermassive black hole is also proportional to the total stellar mass of the galaxy, as well as the stellar mass enclosed in the bulge. By comparing my result to observations from Sahu, Graham, and Davis 2019, it was found that the values from this thesis match the observational data.

In conclusion, adding supermassive black holes into the simulations seems to produce galaxies that resemble observations more closely. Nevertheless, here only three samples of galaxies were considered, where only one of which did not have any SMBHs implemented. It would be interesting to probe a larger sample and thus receive a wider range of galaxy types. This would ultimately lead to a better understanding of how SMBHs affect galaxy formation and evolution.

Appendices

The Impact of Parameters

In a previous section, I described the parameters used for the simulations. Now I would like to take a closer look at how these parameters might affect the outcome of the simulations. To achieve that, another four simulations were run (two with turbulent SMBH accretion and two without) with two slightly different parameters. Run #2 used the same parameters as for the last simulations while only changing `fudge-grad-decent` from 1.0 to 0.1. Run #3 changed `fudge-grad-decent` from 1.0 to 0.5 and `mass-sink-seed` from 10^4 to 10^5 $M_\odot$. In run #3 I also turned on `mass-merger-vel-check-AGN` to 10^6 $M_\odot$ which is the mass above which the two black holes need to be bound first before merging. Even though run #3 has a bit too many changes to draw anything conclusive from, I would still like to take a quick look at it.

To compare these two runs to the previous simulations, some of the same analysis was done for them. The stellar Sérsic indices (Table A.1) for these two runs are a lot lower than for the previous simulations. Especially run #3 seems to be a very dim galaxy. Surprisingly enough, $n_{\mathrm{in},\star}$ is not a lot larger for the turbulent galaxy in run #2, even though in Figure A.2 there was quite a large delay in the mass accretion for the SMBH. This was probably balanced by its black hole having a much larger mass, which in turn makes feedback stronger. One can also see from the Sérsic index of the cold gas mass n_{Gas} that all four galaxies do not have a lot of cold gas left.

	$n_{\mathrm{in},\star}$	n_{gas}	bulge/disk	f_{Gas}	f_{Baryon}
Run #2 SMBH with turb.	2.5±0.1	0.2±0.1	2.2	0.32	0.25
Run #2 SMBH without turb.	2.8±0.1	0.6±0.2	3.7	0.35	0.24
Run #3 SMBH with turb.	0.9±0.1	0.8±0.2	6.1	0.61	0.30
Run #3 SMBH without turb.	1.4±0.2	0.5±0.1	4.3	0.41	0.32

Table A.1: In this table the Sérsic index for the cold gas as well as stellar mass is shown, where for the stellar mass a double Sérsic was used. In addition the bulge to disk ratio as well as the gas and baryon fraction are displayed for the two runs. This was all done at redshift $z = 0$.

In Figure A.1 we can see the circularity for the two runs. The shapes of the four curves as well as their bulge to disk ratio are all very characteristic for an elliptical galaxy. Especially the distributions in run #3 is what I would expect from a purely spheroidal shape. Also, the baryon fraction being between 20% and 40% makes sense. On the other hand, the gas to baryon mass fraction is surprisingly high for an elliptical galaxy since those are usually devoid of any cold gas. This mystery is easily cleared up by looking at the fraction of cold gas to baryonic matter in the galaxy, which is close to zero for all four simulations. This might mean that the AGN feedback has heated up all the gas but not high enough for the majority to escape the galaxy.
All in all, changing the parameters did have an impact on the light and matter profile of the galaxies but did not change their overall morphology.

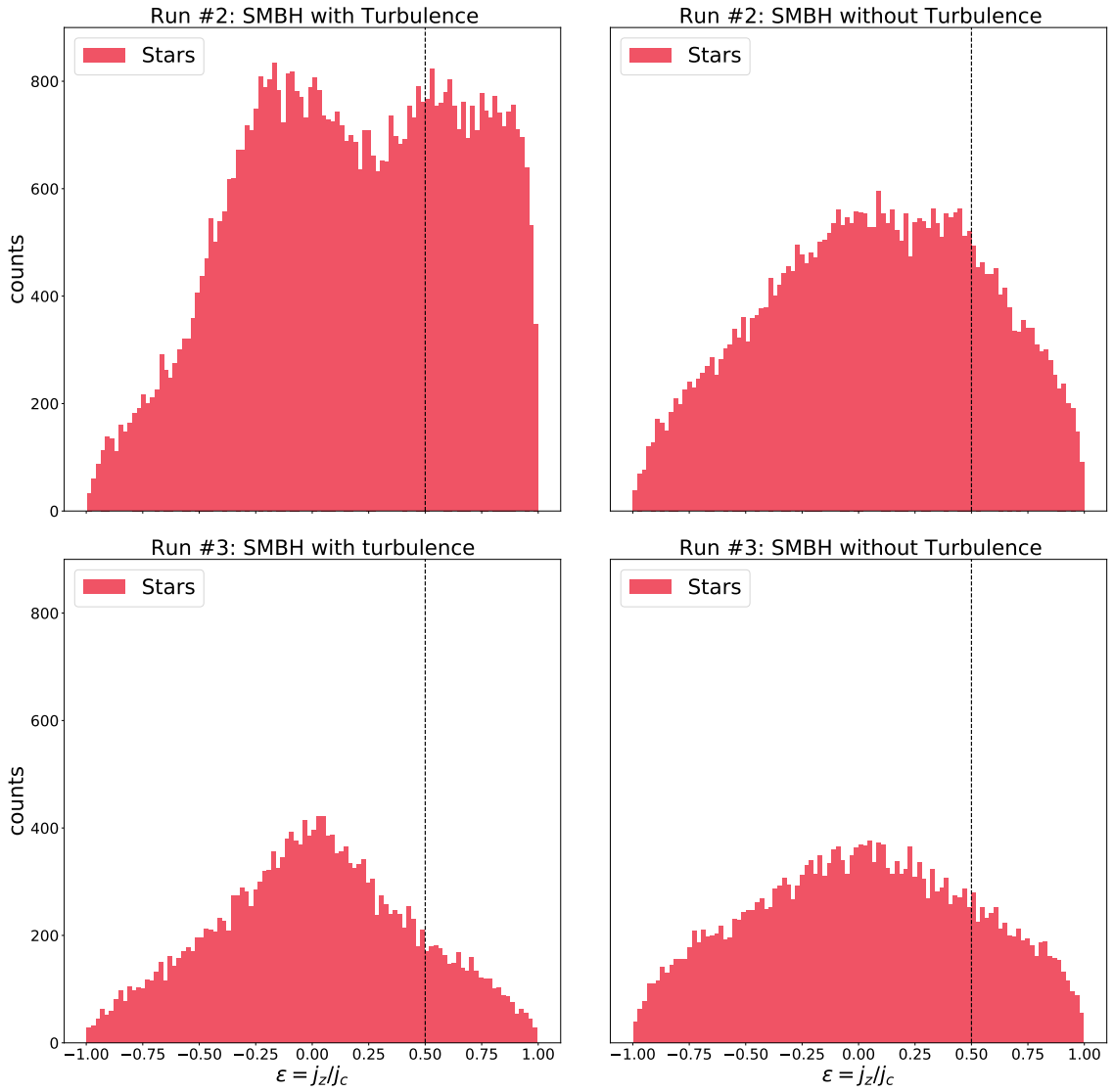


Figure A.1: Above the circularity for the two runs is shown at redshift $z = 0$.

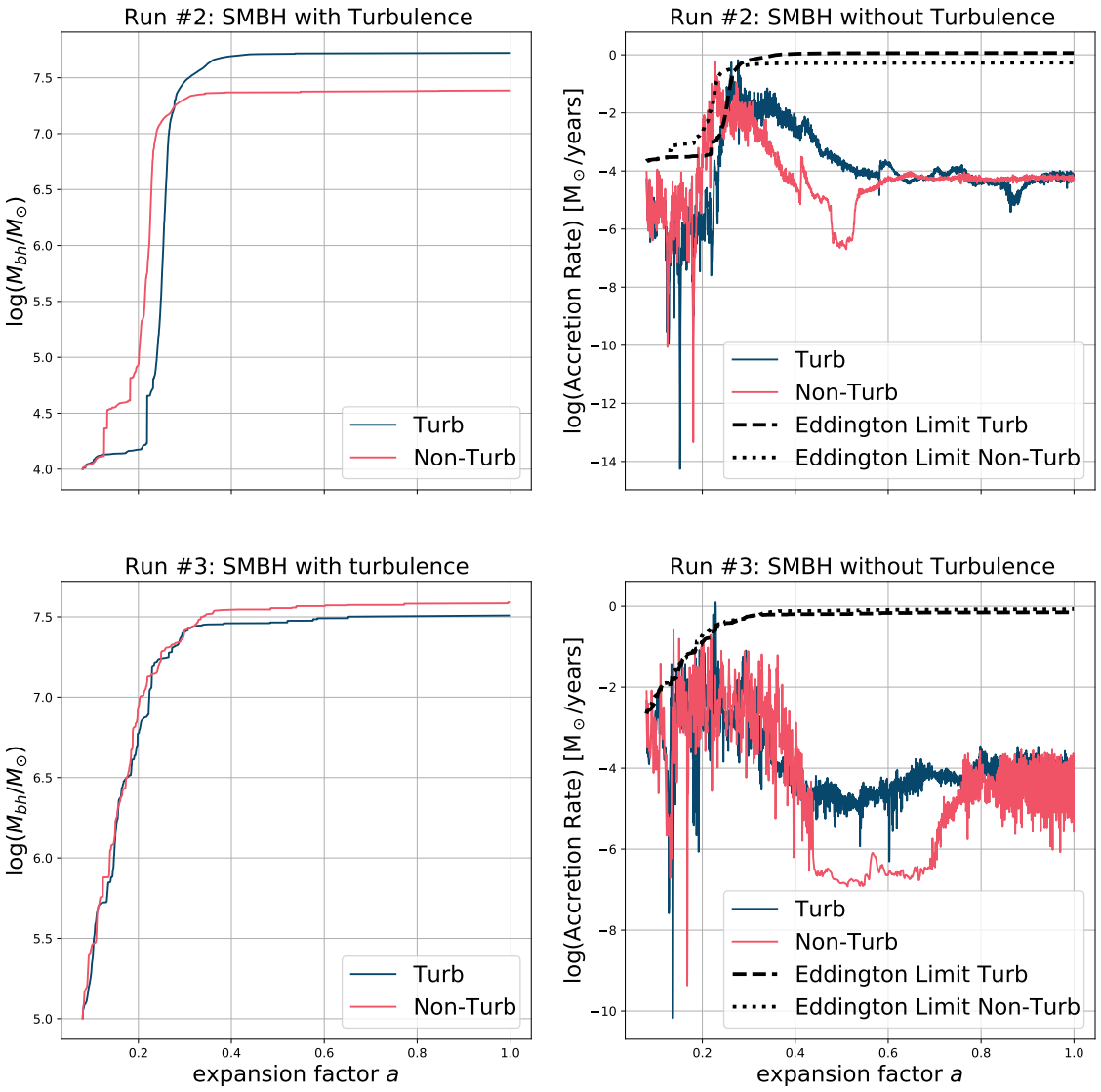


Figure A.2: Above we can see the accretion rate and mass of the SMBH at the centre of the galaxies as a function of the expansion factor a.

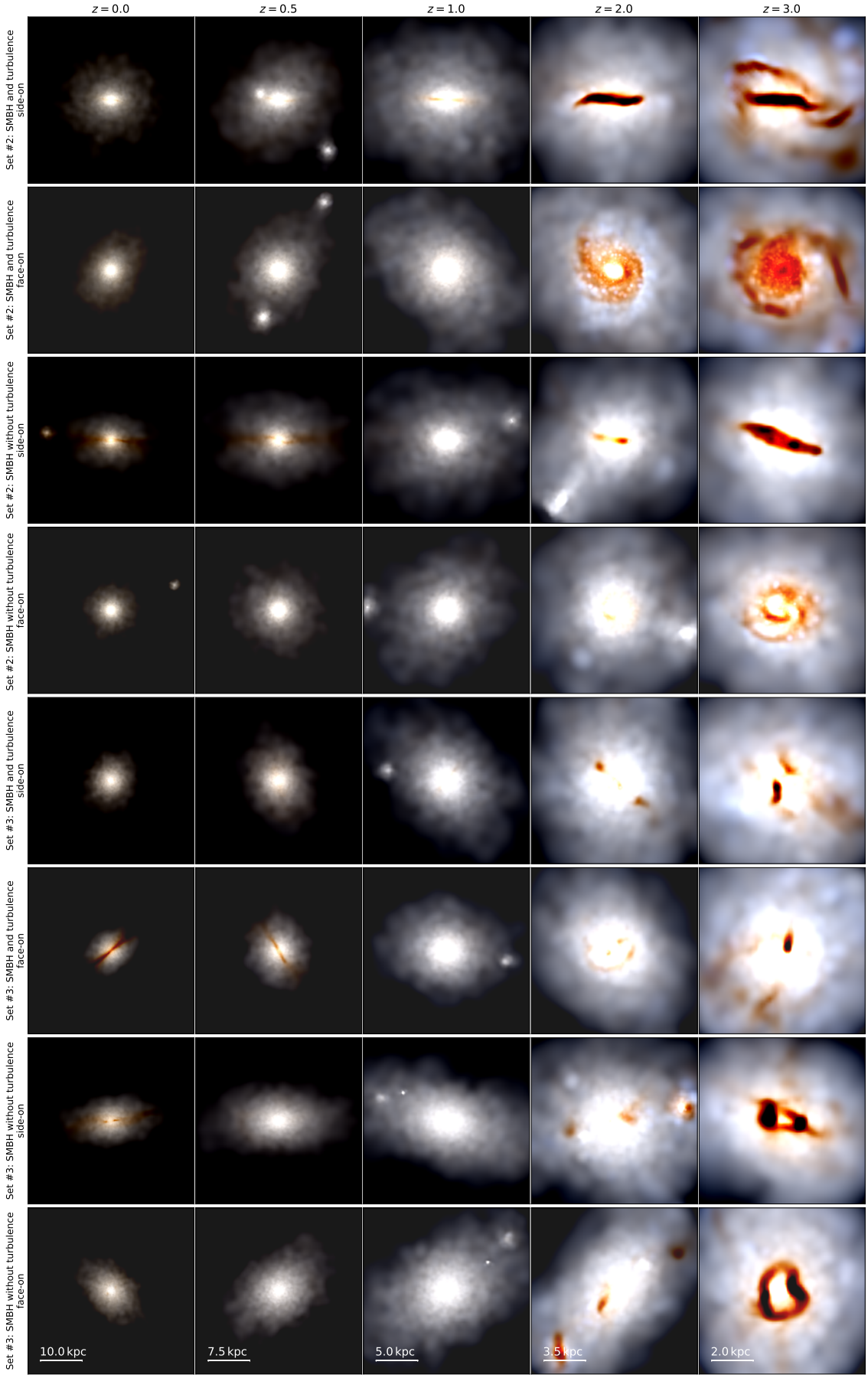


Figure A.3: Above, one can see the true colour renders of the four simulations with different parameters. One can see that all these galaxies seem to be a lot dimmer ellipticals than the SMBH galaxies in the first simulation.

Bibliography

Abadi, Mario G. et al. (Nov. 2003). "Simulations of Galaxy Formation in a Cold Dark Matter Universe. The Fine Structure of Simulated Galactic Disks". In: *Astrophysical Journal* 597.1, pp. 21–34. DOI: 10.1086/378316.

Bate, Matthew R., Ian A. Bonnell, and Nigel M. Price (Nov. 1995). "Modelling accretion in protobinary systems". In: *Monthly Notices of the Royal Astronomical Society* 277.2, pp. 362–376. DOI: 10.1093/mnras/277.2.362. arXiv: astro-ph/9510149 [astro-ph].

Binney, James and Scott Tremaine (2008). *Galactic Dynamics: Second Edition.*

Bleuler, Andreas et al. (June 2015). "PHEW: a parallel segmentation algorithm for three-dimensional AMR datasets. Application to structure detection in self-gravitating flows". In: *Computational Astrophysics and Cosmology* 2, 5, p. 5. DOI: 10.1186/s40668-015-0009-7. arXiv: 1412.0510 [astro-ph.IM].

Bleuler and Teyssier (Nov. 2014). "Towards a more realistic sink particle algorithm for the ramses code". In: *Monthly Notices of the Royal Astronomical Society* 445.4, pp. 4015–4036. ISSN: 0035-8711. DOI: 10.1093/mnras/stu2005. eprint: https://academic.oup.com/mnras/article-pdf/445/4/4015/6092069/stu2005.pdf. URL: https://doi.org/10.1093/mnras/stu2005.

Bromm, Volker and Abraham Loeb (Oct. 2003). "Formation of the First Supermassive Black Holes". In: *The Astrophysical Journal* 596.1, pp. 34–46. ISSN: 1538-4357. DOI: 10.1086/377529. URL: http://dx.doi.org/10.1086/377529.

de Vaucouleurs, Gerard (Jan. 1948). "Recherches sur les Nebuleuses Extragalactiques". In: *Annales d'Astrophysique* 11, p. 247.

Encyclopædia Britannica (2012). *Hubble's system of classification for galaxies.* https://www.britannica.com/science/galaxy/Types-of-galaxies. Accessed: 2021-02-07.

Freeman, K. C. (June 1970). "On the Disks of Spiral and S0 Galaxies". In: *Astrophysical Journal* 160, p. 811. DOI: 10.1086/150474.

Fryer, C. L., S. E. Woosley, and A. Heger (Mar. 2001). "Pair-Instability Supernovae, Gravity Waves, and Gamma-Ray Transients". In: *The Astrophysical Journal* 550.1, pp. 372–382. ISSN: 1538-4357. DOI: 10.1086/319719. URL: http://dx.doi.org/10.1086/319719.

Hahn, Oliver and Tom Abel (July 2011). "Multi-scale initial conditions for cosmological simulations". In: *Monthly Notices of the Royal Astronomical Society* 415.3, pp. 2101–2121. ISSN: 0035-8711. DOI: 10.1111/j.1365-2966.2011.18820.x. URL: http://dx.doi.org/10.1111/j.1365-2966.2011.18820.x.

Häring, Nadine and Hans-Walter Rix (Apr. 2004). "On the Black Hole Mass-Bulge Mass Relation". In: *The Astrophysical Journal* 604.2, pp. L89–L92. DOI: 10.1086/383567. arXiv: astro-ph/0402376 [astro-ph].

Hubble, E. P. (Dec. 1926). "Extragalactic nebulae." In: *Astrophysical Journal* 64, pp. 321–369. DOI: 10.1086/143018.

Khokhlov, A.M (July 1998). "Fully Threaded Tree Algorithms for Adaptive Refinement Fluid Dynamics Simulations". In: *Journal of Computational Physics* 143.2, pp. 519–543. ISSN: 0021-9991. DOI: 10.1006/jcph.1998.9998. URL: http://dx.doi.org/10.1006/jcph.1998.9998.

Kretschmer, Michael and Romain Teyssier (Dec. 2019). "Forming early-type galaxies without AGN feedback: a combination of merger-driven outflows and inefficient star formation". In: *Monthly Notices of the Royal Astronomical Society* 492.1, pp. 1385–1398. ISSN: 1365-2966. DOI: 10.1093/mnras/stz3495. URL: http://dx.doi.org/10.1093/mnras/stz3495.

Mo, Houjun, Frank van den Bosch, and Simon White (2010). *Galaxy Formation and Evolution*. Cambridge University Press. DOI: 10.1017/CBO9780511807244.

Montero, Pedro J., Hans-Thomas Janka, and Ewald Müller (Mar. 2012). "RELATIVISTIC COLLAPSE AND EXPLOSION OF ROTATING SUPERMASSIVE STARS WITH THERMONUCLEAR EFFECTS". In: *The Astrophysical Journal* 749.1, p. 37. ISSN: 1538-4357. DOI: 10.1088/0004-637x/749/1/37. URL: http://dx.doi.org/10.1088/0004-637X/749/1/37.

Penzias, A. A. and R. W. Wilson (July 1965). "A Measurement of Excess Antenna Temperature at 4080 Mc/s." In: *Astrophysical Journal* 142, pp. 419–421. DOI: 10.1086/148307.

Sahu, Nandini, Alister W. Graham, and Benjamin L. Davis (May 2019). "Black Hole Mass Scaling Relations for Early-type Galaxies : $M_{BH} - M_{\star,sph}$ and $M_{BH} - M_{\star,gal}$". In: *The Astrophysical Journal* 876.2, p. 155. ISSN: 1538-4357. DOI: 10.3847/1538-4357/ab0f32. URL: http://dx.doi.org/10.3847/1538-4357/ab0f32.

Sérsic, J. L. (Feb. 1963). "Influence of the atmospheric and instrumental dispersion on the brightness distribution in a galaxy". In: *Boletin de la Asociacion Argentina de Astronomia La Plata Argentina* 6, pp. 41–43.

Shu, Frank H. (1991). *Physics of Astrophysics, Vol. I.*

Swinburne University of Technology (2021). *Population III*. URL: https://astronomy.swin.edu.au/cosmos/p/Population+III (visited on 02/05/2021).

Teyssier, R. (Apr. 2002). "Cosmological hydrodynamics with adaptive mesh refinement. A new high resolution code called RAMSES". In: *Astronomy and Astrophysics* 385, pp. 337–364. DOI: 10.1051/0004-6361:20011817. arXiv: astro-ph/0111367 [astro-ph].

The Infinite Loop (2014). *Advanced Octrees 1: preliminaries, insertion strategies and maximum tree depth*. https://geidav.wordpress.com/2014/07/18/advanced-octrees-1-preliminaries-insertion-strategies-and-max-tree-depth/. Accessed: 2021-02-16.

Yu, Q. and S. Tremaine (Oct. 2002). "Observational constraints on growth of massive black holes". In: *Monthly Notices of the Royal Astronomical Society* 335.4, pp. 965–976. ISSN: 1365-2966. DOI: 10.1046/j.1365-8711.2002.05532.x. URL: http://dx.doi.org/10.1046/j.1365-8711.2002.05532.x.